Selection of representative volume elements for pore-scale analysis of transport in fuel cell materials

E.A. Wargo [a,b], A.C. Hanna [a,b], A. Çeçen [a,b], S.R. Kalidindi [b], E.C. Kumbur [a,*]

[a] Electrochemical Energy Systems Laboratory, Department of Mechanical Engineering and Mechanics, Drexel University, Philadelphia, PA 19104, USA
[b] Mechanics of Microstructures Group, Department of Mechanical Engineering and Mechanics, Department of Materials Science and Engineering, Drexel University, Philadelphia, PA 19104, USA

ABSTRACT

Pore-scale modeling has become a quite popular tool for evaluating the impact of material structure on fuel cell performance. However, the computational complexity of these models often limits simulations to analyze only a small volume of material, which is typically selected randomly from a much larger microstructure dataset. When considering the heterogeneous internal structure of fuel cell materials, it is highly unlikely that such a randomly selected volume (i.e., model domain) would adequately reflect the salient features of the material structure. The objective of this work is to utilize the recent advances in microstructure quantification to select *small* representative volume elements (RVEs) that accurately reflect the overall microstructure and transport properties of fuel cell materials. The microporous layer (MPL) in polymer electrolyte fuel cells is chosen for initial demonstration of the approach. Dual-beam focused ion beam scanning electron microscopy is utilized to obtain a 3-D structural dataset of the selected MPL sample. The RVEs are selected using the new approach of weighted sets of optimally selected statistical volume elements, and the key structure and transport metrics are evaluated using advanced microstructure algorithms developed in-house. Metric comparisons between the RVEs and the full dataset indicate that the RVEs selected by this approach offer a very good representation of the full dataset, albeit in a volume that is *significantly smaller* in spatial extent, therefore providing a computationally efficient and reliable model domain for pore-scale analyses.

© 2011 Elsevier B.V. All rights reserved.

1. Introduction

With the potential for high power density and efficiency, fuel cells hold great promise for powering many applications. Current research efforts for fuel cells are focused on improving their durability and performance, both of which are inherently influenced by the materials used in these systems [1]. The properties and transport behavior of these materials are strongly linked to their unique and complex internal structure (henceforth referred to as "microstructure"). As a result, significant effort has been devoted to characterize the microstructure of these materials. Due to the minute length scales and heterogeneous nature of many fuel cell materials, experimental investigations can be expensive and quite difficult to conduct, if not impossible. Consequently, modeling studies have become an indispensable tool for investigating the effects of these materials on the overall system performance and durability.

Although existing modeling efforts have greatly advanced the level of our understanding regarding fuel cell operation, certain phenomena are yet to be fully explained. For instance, water management is a critical issue which continues to plague polymer electrolyte fuel cell (PEFC) development [1–10]. Numerous modeling studies have been performed to investigate the water transport and distribution in PEFC materials (e.g., diffusion media, catalyst layer, etc.) [2,5,6,8,9,11–41]. Although these efforts provide valuable insights, major discrepancies still exist between the experimental and modeling studies. These inconsistencies likely originate from the fact that the microstructure features of the fuel cell materials are not accurately accounted for in the current modeling efforts. For instance, macroscopic models are often fast and quite useful; however, most of them rely heavily on bulk correlations adopted from other fields, which do not adequately account for the specific microscale topology in most fuel cell materials [3,41].

Alternatively, pore-scale modeling can rectify the deficiencies of macroscopic modeling, as it can be applied directly to more realistic representations of the internal structure of PEFC materials. However, each pore-scale modeling technique has its own limitations. For instance, pore network modeling (PNM) is fairly

* Corresponding author. Tel.: +1 215 895 5871; fax: +1 215 895 1478.
  E-mail addresses: kumbur@drexel.edu, eck32@drexel.edu (E.C. Kumbur).

computationally efficient [11–18], but utilizes highly idealized geometrical descriptions of the material's pore space. For example, the diffusion media (DM) in PEFCs is often represented as an arrangement of pores, throats and solid on a cubic lattice [11–14]. While such idealization dramatically reduces the computational time, the applicability of using such simplified geometries in predicting the transport through the DM internal structure is highly questionable. Recently, a few studies have attempted to better represent the material by randomizing the location of the structural features in the pore network [15–18]. Hinebaugh et al. [18] went a step further by accounting for through-plane heterogeneity in porosity based on X-ray computed tomography (XCT) data. Despite progress, more work is still needed to improve the resolution of these models to accurately capture the true material structure and related effects on the cell performance.

Recently, other pore-scale approaches have emerged that can be applied to more realistic material structures, such as those obtained using 3-D imaging techniques like XCT or focused ion beam scanning electron microscopy (FIB-SEM). A promising approach is the lattice-Boltzmann (LB) method [19–21]. In the last five years, the LB method has been successfully utilized to investigate transport phenomena in fuel cells, especially in the DM of PEFCs [22–32]. Although these studies offer significant insight into the multiphase transport in DM, many of these models were actually built on virtual stochastic microstructures based on 2-D SEM micrographs and other data [22–28]. More recently, a few LB-based modeling efforts have been reported which utilize 3-D microstructure data of fuel cell DM obtained from XCT and FIB-SEM [29–32]. However, since the LB method is fairly computationally intensive, these models were limited to analyze very small sub-volumes ($\sim$50–150 pixels^3 selected either randomly or by some generic averaging process) of the full dataset (over $\sim$ 500 pixels^3), which may or may not accurately reflect the overall microstructure of the DM. Considering the complex structure of fuel cell DM, it is very likely that selection of "random" small volumes will not accurately reflect the overall microstructure of the DM and result in inaccurate conclusions regarding the structure–transport–performance relationship. Similar issues also exist for other pore-scale approaches. For instance, the volume of fluid (VOF) method has been recently employed to simulate multiphase transport in PEFCs [33–40]. Due to the computational complexity, the VOF method is also limited to modeling the transport through small volume sizes.

Pore-scale modeling techniques such as the LB and VOF methods show tremendous promise for overcoming the major limitations of macroscopic and pore network modeling. However, the high computational costs associated with these methods restrict them to analyses of relatively small volumes which are selected from the full material dataset either randomly or by some generic averaging process. Here, we show that choosing such small volumes "randomly" from the full dataset is unlikely to yield results which are representative of the full dataset. Therefore, a more rigorous approach is needed to select a proper representative volume element (RVE) from the full dataset that accurately represents the prominent features of the material for reliable model simulations.

The concept of an RVE is commonly invoked in studying important microstructure–property relationships in materials science. An RVE is defined as a finite region in the material structure that is "statistically representative" of the entire sample's microstructure and represents the macroscale properties of the sample with a desired accuracy [42–44]. In practice, the *size* of a single RVE representing the entire microstructure is typically too large to allow detailed microscale simulations with sophisticated physics-based models. Alternatively, it is possible to capture the important details of the microstructure in a set of small randomly selected statistical volume elements (SVEs) [45–47]. However, this approach requires a fairly large number of SVEs to accurately capture the important

details of the microstructure. Recognizing these challenges, Niezgoda et al. [42] have recently proposed the novel concept of a weighted set of optimally selected SVEs, referred to as a "WSVE Set", to determine the proper RVEs that accurately reflect the overall microstructure features of the material of interest. The resulting RVEs are significantly smaller in spatial extent than the full dataset, and therefore are more computationally efficient. The WSVE Set approach was applied to different composite materials, and validated in terms of efficiently capturing selected microstructure metrics and mechanical properties of the various composite materials [42].

The objective of this study is to explore the ability of the WSVE Set approach to accurately capture the important structural features and related transport properties of fuel cell materials in small representative volumes. For demonstration purposes, the WSVE Set approach is applied to the micro-porous layer (MPL) in PEFCs to select small RVEs which accurately reflect the prominent features of a much larger MPL microstructure dataset. Results indicate that the RVEs selected by this approach offer a very good representation of the full dataset in a volume that is significantly smaller in spatial extent than the full dataset, therefore providing a computationally efficient and reliable model domain for pore-scale modeling efforts.

2. Method of approach

The method to choose the proper RVE Sets for the tested MPL sample consists of four main steps: (a) microstructure dataset acquisition, (b) data pre-processing and segmentation, (c) full dataset construction and RVE selection, and (d) detailed structure and property analysis of the full dataset and selected RVEs (i.e., RVE validation). Each step is described in detail below, and a flow chart outlining the main steps of the present study is shown in Fig. 1.

2.1. Dataset acquisition

As a first step to study the MPL microstructure, an FEI Strata^{TM} DB 235 FIB-SEM was utilized to perform nanotomography on the MPL of a SIGRACET® SGL 10 BC gas diffusion layer. The FIB-SEM technique incorporates both a focused ion beam and an electron beam in a single system, and can be used to provide high quality volumetric and cross-sectional images of the tested samples [31,48,49]. The high precision beam control/ion-milling ability enables serial cross-sectional surface slicing, which is used for 3-D visual reconstruction of the tested specimen. In this study, prior to any milling with the Ga$^+$ ion beam, a 1.5 μm platinum layer was deposited over the target volume of interest to prevent ion damage. The volume of interest was then exposed as a peninsula by milling away the surrounding volume (Fig. 2a and b). Sectioning the end face of this peninsula (rather than one face of a rectangular pit milled into the MPL surface, as is commonly performed [31,48]) allows for minimizing the horizontal gradients and prevents image darkening with successive cross sections, both of which complicate image processing and segmentation. Serial cross-sectional micrographs of the MPL were obtained by successively milling 20 nm slices at 500 pA/30 kV, followed by capturing an SEM image of the milled surface (Fig. 2c). To maximize image clarity and achieve a pixel resolution of $\sim$10 nm, the SEM was operated in ultrahigh-resolution mode using a through-the-lens detector. Tomographic data was obtained in this manner from four different locations on the MPL sample to capture any spatial heterogeneity within the material structure. At each location, a total of 150 slices were milled and imaged, which resulted in a captured volume of $\sim$5 μm $\times$ 8 μm $\times$ 2 μm from each of the four data sampling locations.
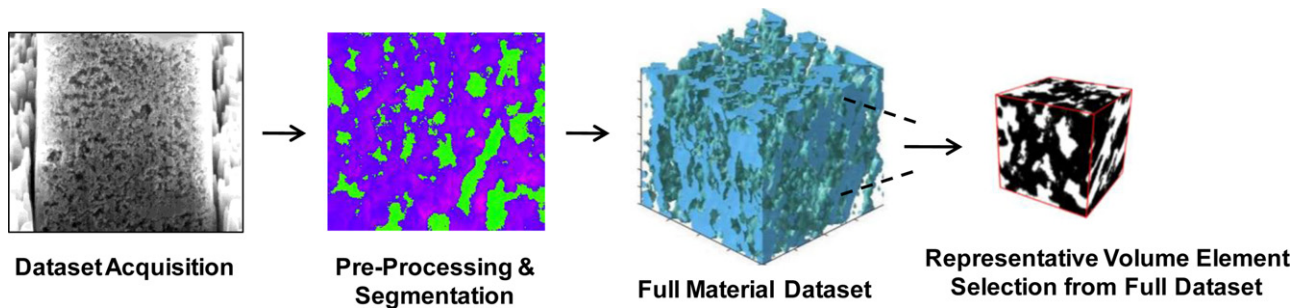
Fig. 1. Flow chart outlining the main steps of the present study.

2.2. Image pre-processing

The next step is to pre-process all the images to ensure accurate quantification of the internal structure of the tested MPL. The raw FIB-SEM image sets are inherently problematic, due to the off-normal angle of the SEM source and the small pore sizes in the MPL which approach the limits of FIB-SEM resolution. To address these issues, we have developed a specific image pre-processing protocol using the MATLAB Image Processing Toolbox [50] and the MATLAB Central online code repository. The data pre-processing protocol has four main steps: (i) image alignment, (ii) viewing angle correction, (iii) creation of cubic voxels, and (iv) gradient removal.

A relatively high SEM magnification is necessary to capture the nanoscale features of the MPL structure. Consequently, any small change in the SEM viewing area due to beam shift and/or sample drift can translate to significant in-plane image displacements between successive image slices. To correct for any misalignment within the image stack, a discrete Fourier transform registration code [51,52] is applied at the sub-pixel level, by using regions of the image outside the cross-sectional face as fiduciary markers. Another challenge which arises in image processing is for the correction of the off-normal viewing angle ($\theta = 52°$) between the SEM source and the cross-sectional surface being imaged (Fig. 2d and e). Because the electron beam is not incident perpendicular to this surface, the top edge of the sectioned region appears to creep upward in successive images. This can be corrected by shifting each image downward by a number of sub-pixels, s:

$$S = \frac{t}{p} \cos \theta \qquad (1)$$

which depends on the slice thickness t (nm), the pixel size p (nm pixel^{-1}), and the viewing angle θ [49]. Following downshift, the image must also be stretched vertically by a factor f to account for the angular projection [49]:

$$f = \frac{1}{\sin \theta} \qquad (2)$$

Once all images have been properly aligned and stretched, the entire stack of images is cropped so that only the desired internal structural information remains. Fig. 3 outlines the image pre-processing steps described up to this point.

It is often convenient to convert the datasets into volumes composed of cubic voxels for further evaluation of structure metrics (i.e., properties) to determine the overall transport characteristics of the tested sample. Since the slice thickness is generally larger than the pixel dimensions in the images, stretching and interpolating the image stack in the through-plane direction is required to achieve sufficient image clarity. Despite the advantage of serially cross-sectioning a peninsula, the raw images inevitably contain slight shadow gradients (Fig. 4a). These gradients tend to lower the accuracy of image segmentation. We have removed the gradients in the raw images by performing a bi-parabolic fit to each

grayscale image and then dividing the image data by the fitted bi-parabolic surface (Fig. 4a). The bi-parabolic fit was computed using the surface fitting code by Pastushenko [53].

2.3. Segmentation

Following image pre-processing, the next important task is to develop and implement an appropriate segmentation protocol for the particular microstructure dataset to enable accurate determination of whether each pixel is occupied by the solid or the pore phase (only one is allowed in each pixel). The solid phase in tested MPL samples actually consists of several distinct phases (e.g., hydrophilic carbon particles, hydrophobic polytetrafluoroethylene). These hydrophobic/hydrophilic phases cannot be distinguished in the FIB-SEM datasets, therefore the segmentation process presented in this paper does not account for the local wettability as a separate phase in the MPL microstructure.

It is very challenging to determine the accuracy of a given segmentation technique on the datasets due to the fact that the MPL is formed as a thin layer deposited on the macro-DM surface. Consequently, porosity in the MPL is not readily measurable, and can only be estimated through comparing the porosity measurements of macro-DM substrate with the measured values for MPL-coated DM by assuming an MPL thickness range ($\sim$50–100 μm) [54]. These estimates yield a porosity value for the MPL in the range of $\sim$0.4–0.6, which agrees with mercury intrusion porosimetry data for other MPL samples reported in literature [55], but is still too broad to be used for precise calibration of the segmentation techniques employed. Beyond a rough expectation of adherence to this range, the only other criteria for selection of a particular segmentation technique is careful visual inspection of the segmentation results.

Since the MPL has a highly heterogeneous structure with small pores, accurate separation of pore and material regions in the captured images presents a significant challenge, as irregularities in shadowing can make it extremely difficult to distinguish between the two. Large scale variations in mean brightness across the image are mostly eliminated by the shadow gradient removal procedure described above. However, even with this correction, it is still possible for a pixel which really represents a pore region to have the same brightness as another pixel which should be counted as a material region. The difficulty of distinguishing the pore and material phases is illustrated by the histograms in Fig. 4b. Ideally, one would prefer that the pore and material pixels in each image display a bi-modal distribution, such that the pore pixels form a distinct cluster (peak) around some dark grayscale value, while the material pixels form a distinct bright cluster. In Fig. 4b, an example of an ideal distribution is shown in red (dashed); however, the true case is generally more like the histogram shown in blue (solid), which lacks distinct peaks and shows only a hint of a "shoulder" on the left side of its single peak. (For interpretation of the references to color in the text, the reader is referred to the web version of the article.) A sensible
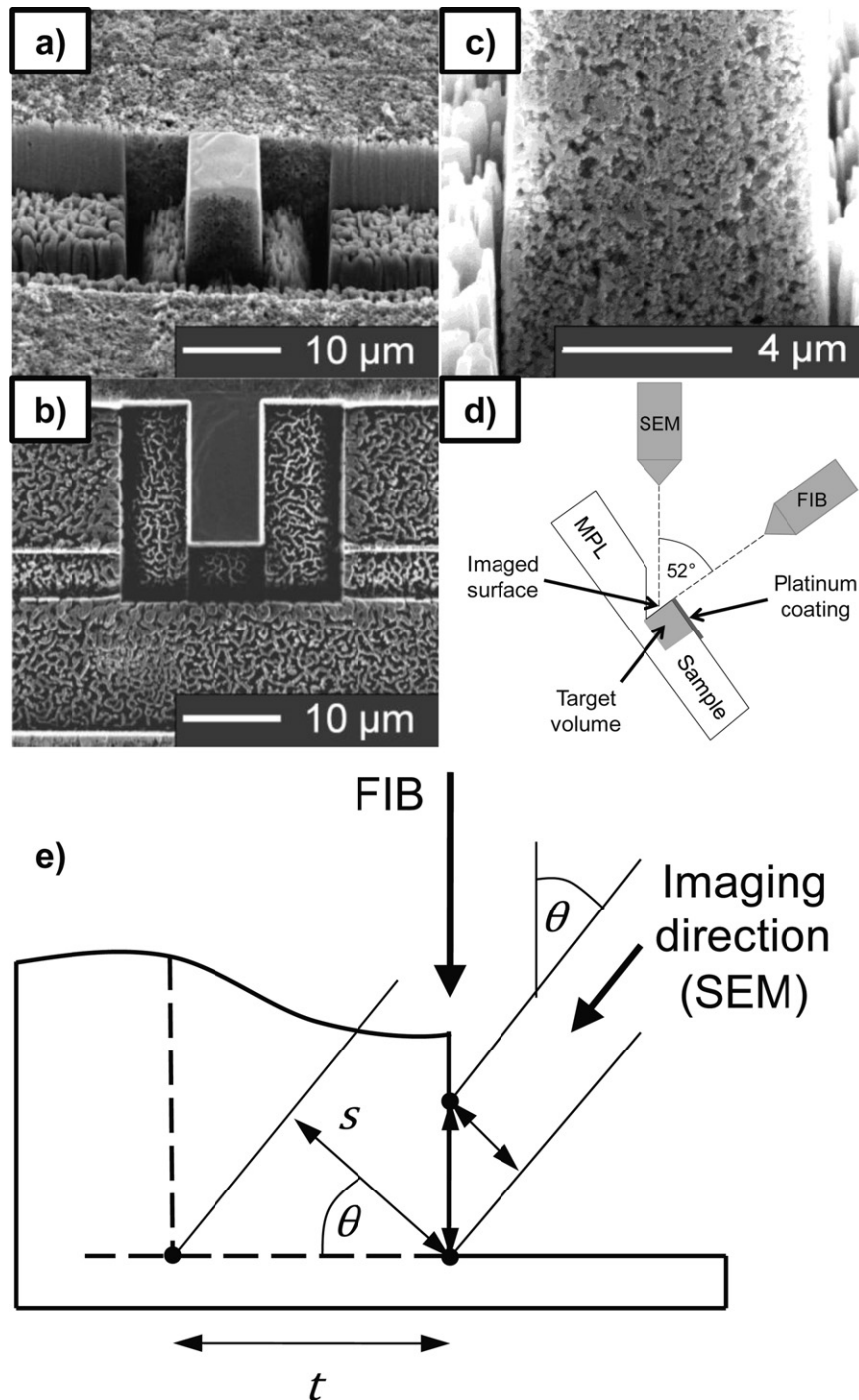
Fig. 2. Serial-sectioning of the MPL using FIB-SEM. (a) 52° view SEM image, (b) top view FIB image, (c) example cross section slice, close up at 52°, (d) schematic of FIB-SEM configuration (adapted from Iwai et al. [48]), and (e) SEM image projection effects Adapted from Inkson et al. [49].

assumption might be that the location of this shoulder represents a reasonable dividing line between pore and material pixels, but applying this assumption 'manually' (after equalizing brightness histograms across all images in a set) gives an unexpectedly low mean porosity (in the range of 0.22 ± 0.12) for the MPL sample, and clearly misidentifies pore pixels as material pixels upon visual inspection (Fig. 4c).

To overcome the limitation of manual thresholding, we have performed automatic threshold selection techniques such as the iterative ISODATA method [56–58] and Otsu's method [59]. The iterative ISODATA method uses the mean grayscale value of the image as an initial guess at the threshold, computes the mean brightness of the pixels to either side of this threshold, and averages these two values to compute its next guess at the threshold. This process is repeated until the threshold level changes by less than some specified tolerance. Otsu's method seeks a grayscale threshold that minimizes the intra-class brightness variance, defined as a weighted sum of the brightness variances within each of the two classes [59]. The weighting factor is equal to the fraction of the image pixels which fall within each class. The minimization is performed by exhaustively computing the intra-class
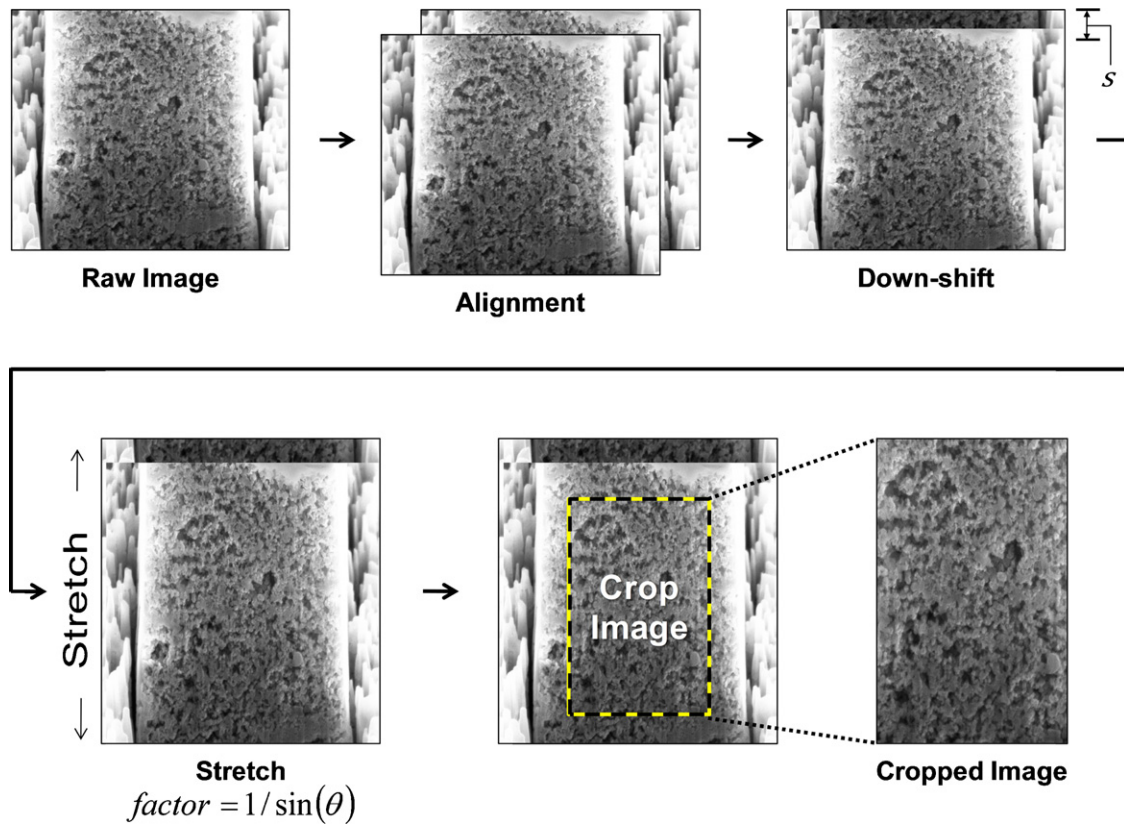
Fig. 3. Flow chart outlining the initial image pre-processing steps for the FIB-SEM dataset.

brightness variance across all possible threshold values and selecting the threshold which gives the best result.

For our particular microstructure dataset, the iterative ISODATA method (Fig. 4c) and Otsu's method yield porosity values of 0.42 ± 0.02 and 0.43 ± 0.02, showing a good agreement with each other. The segmented images arising from these methods are almost indistinguishable. Since the difference between these two well-established techniques is substantially less than the variations we might expect due to other sources of error (detection error, material redeposition on the surface, etc.), the ISODATA thresholding method [56–58] was chosen in this study for segmentation and further analysis of the captured images. Once segmentation was complete, the stack of binary images was combined in 3-D, forming a volumetric reconstruction of the measured microstructure (Fig. 5).

2.4. Representative volumes

Once the microstructure of the tested MPL sample was captured and properly segmented to obtain a 3-D dataset, the full dataset was analyzed to select an RVE. In this study, we employed the novel WSVE Set approach [42] which captures the details of the microstructure in a set of small volumes that are optimally selected from the larger, full dataset. In this approach, the statistical volume elements (SVEs) in the set are chosen using optimization algorithms, and they are individually weighted to best capture the selected microstructure metrics (in this case 2-point statistics, explained below) of the full dataset. Therefore, the resulting set of weighted SVEs serves as an equivalent of an RVE (Fig. 6). The macroscale effective value for any property ("metric") of the given material is calculated by taking the weighted average of the corresponding values for the members of the WSVE Set. The number of

volume elements in the WSVE Set is selected such that the measured ensemble-averaged 2-point statistics of the full dataset are matched within acceptable tolerance [42,44].

In this work, we followed the same approach where the WSVE Sets for the MPL sample were extracted such that they reflect the ensemble-averaged 2-point statistics of the full MPL dataset with high accuracy. A 2-point statistic (or 2-point correlation) captures the spatial correlation between two different local states (e.g., phases) present in the structure [43,60]. More specifically, a 2-point correlation shows the probability for which the head and tail (i.e., "two points") of a vector (of specific orientation, placed within the 3-D dataset) lie in particular phases (e.g., pore, solid material). When the same local state is selected for both ends of the vector (i.e., head and tail), the 2-point correlation is referred to as an auto-correlation. However, if different local states are selected for the ends of the vector, the 2-point correlation is called a cross-correlation. When considering a pore–pore auto-correlation for example, both the head and the tail of the vector must lie in the pore phase of the material.

The 2-point statistics are used here to capture the important statistical measures of the structure, since they contain significant information regarding the shape, size, and spacing of features (i.e., phases) within the microstructure [61,62]. As an example, a 3-D two-phase microstructure volume composed of $100 \times 100 \times 100$ voxels requires 100^3 2-point statistics (dimensions) to represent it. The specific importance of any one of these statistics varies based on the structural features of the material under investigation. For this particular problem, to speed up the WSVE Set selection process, this large amount of data is adequately represented in a much lower dimensional space using principal component analysis (PCA). The PCA method decomposes the data into an orthonormal basis, ranked by order of importance [42]. In
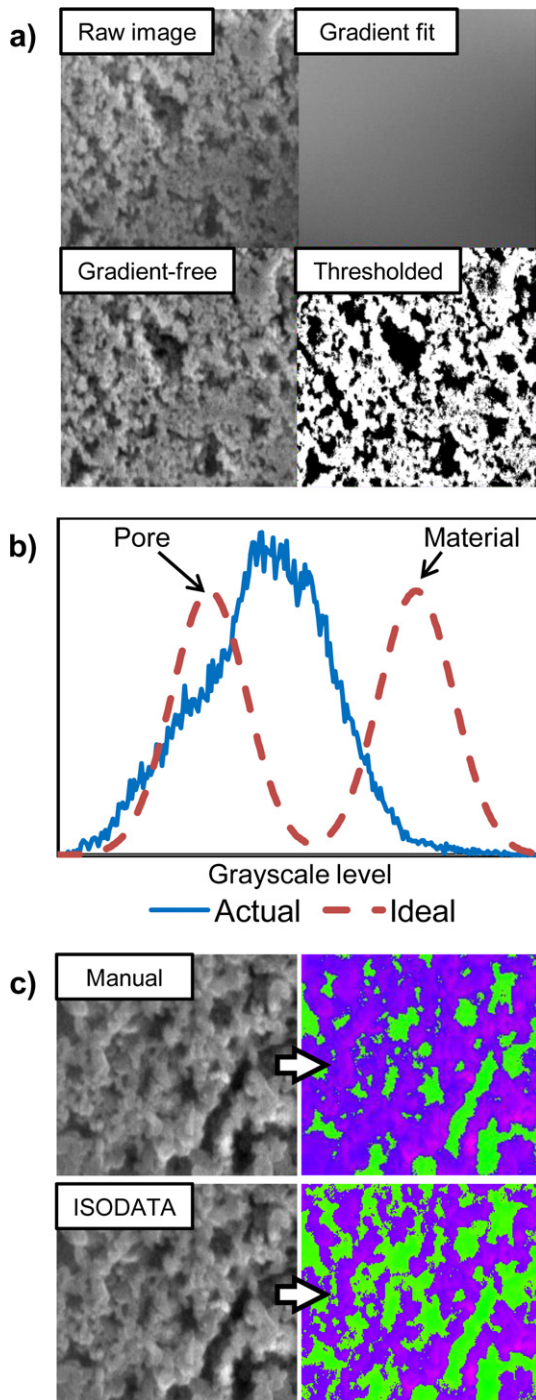
Fig. 4. (a) Pre-processing stages of raw FIB-SEM images of the tested MPL sample, showing the raw image, gradient fit, gradient-free image, and thresholded image with pore space shown in black. (b) Ideal vs. actual image histogram, showing the challenge of distinguishing the pore and material peaks (phases). (c) Image segmentation by thresholding via manual inspection and the iterative ISODATA method [56–58].

the high dimensional space, the direction with the greatest scatter is chosen as the principal direction. Then, all directions normal to the principal direction are examined to find the one(s) with the most scatter. Often, only a few basis vectors are necessary to provide an adequate representation. For this particular problem, the specific weight of each SVE member is optimally assigned during the PCA procedure so that the 2-point statistics are best matched by the WSVE Set.

Since the properties of a material are complicated functions of its underlying structure, it is expected that an RVE that captures the structure well (e.g., through the 2-point statistics) will also accurately represent the effective material properties [42]. For the measured MPL datasets, since only two phases (solid and pore) are considered, there is only one independent 2-point correlation. For convenience, this independent 2-point correlation was selected as the pore–pore auto-correlation in this study.

2.5. Evaluation of key structural properties (metrics) for WSVE Set validation

Once a WSVE Set is selected from the full microstructure dataset, the next step is to validate the WSVE Set through a detailed comparison of key structure metrics calculated for the WSVE Set and the full material dataset. Several key microstructure metrics have been identified for this purpose, which include the porosity, internal surface area, connected internal surface area, tortuosity, and structural diffusivity coefficient. Although these metrics are used primarily to validate the WSVE Sets produced in this work, many of them are also of high importance for PEFC modeling studies. All of these key metrics were calculated via special algorithms developed in-house. More detailed information may be found in our publication [63].

The key structure related metrics of porosity and internal surface area were estimated using fundamental image analysis techniques. Porosity was calculated by taking the ratio of the number of pore voxels to the total number of voxels in the tested 3-D volume. Internal surface area was estimated by detecting phase boundaries in the three primary orthogonal directions. The resulting count of boundary voxels was multiplied by the surface area of a voxel face and then divided by the size of the tested volume to estimate the internal surface area per unit volume. The connected surface area per unit volume was calculated in a similar fashion; however, any pore voxels that were isolated from the through-plane connected pore network were neglected.

In particular, we have taken a unique approach for the estimation of two important transport related metrics: (i) tortuosity and (ii) the structural diffusivity coefficient. Tortuosity was estimated by using Dijkstra's search algorithm [64] in 3-D, to identify the shortest path between a designated voxel on one face of the sample volume and the opposing face (Fig. 7a) [63]. Rather than utilizing an effective diffusion coefficient-tortuosity correlation based on diffusion simulations as in [31,48], our procedure calculates the tortuosity by comparing the identified shortest path lengths for every single pore voxel on one face to the shortest distance between the opposing surfaces. The tortuosity analysis was performed specifically in the primary flow direction of interest (e.g., through-plane direction) by examining the shortest path from every pore voxel on the start surface to the destination surface of the tested material volume. This analysis results in a tortuosity distribution, which provides a great deal of detail regarding the tortuous nature of the transport paths in the material of interest. As such, an effective tortuosity value for the tested material structure can be determined by the detailed analysis of the tortuosity distribution.

A 3-D diffusion model has been developed in-house to evaluate the structural diffusivity coefficient, based on a finite volume approximation of the steady-state Fickian diffusion model [63]. Appropriate boundary conditions were used to impose zero flux on the lateral surfaces, and uniform but different concentrations on the top and bottom surfaces (i.e., the start and end surfaces used in the through-plane tortuosity estimation), respectively. Fig. 7b shows the resulting steady-state concentration field within the porous structure of the MPL reconstruction. Estimates for the effective diffusivity and the structural diffusivity coefficient can be easily obtained from the resulting value of the net flux [63]. The structural
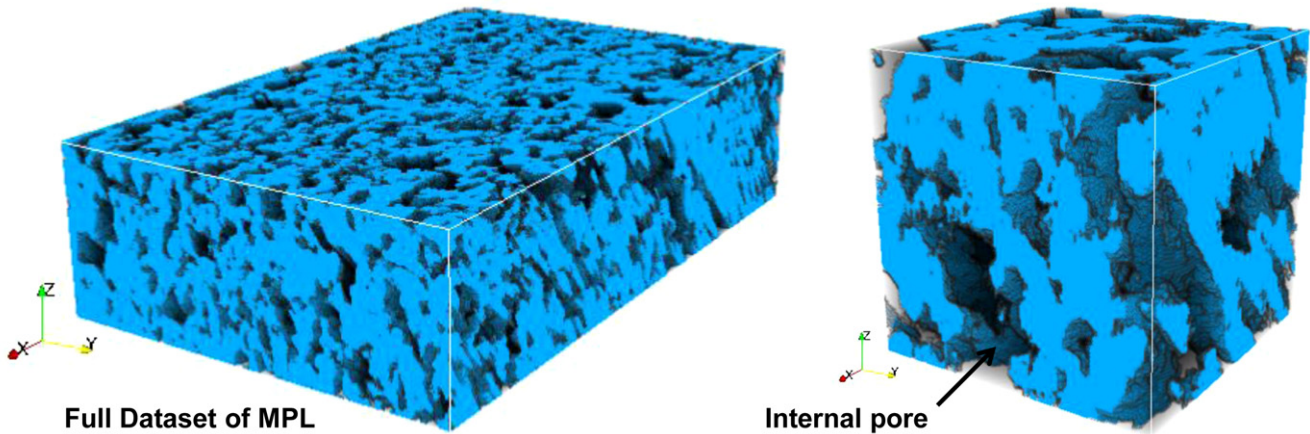
Fig. 5. Three-dimensional reconstruction of the measured MPL microstructure. One full dataset is shown on the left ($500 \times 800 \times 204$ pixels, or $\sim 5\,\mu m \times 8\,\mu m \times 2\,\mu m$). A $100\,pixel^3$ volume is shown on the right to better visualize the MPL pore structure.

diffusivity coefficient is selected here as an example of a basic bulk transport property that is expected to be significantly influenced by the details of the microstructure. More detailed information regarding the determination of the structural diffusivity coefficient can be found in [63].

3. Results and discussion

3.1. Data selection and spatial variance of microstructure in MPL

In order to examine if there are significant spatial variations in the microstructure (from one location to another in the MPL), a total of four large datasets (referred to as full datasets) were extracted via FIB-SEM as described earlier. A detailed screening procedure was then performed to investigate the degree of structural variation between the four datasets by comparing their 2-point statistics. The dataset comparison was conducted as follows:

300 random volumes of window size $100 \times 100 \times 100$ pixels ($100\,pixels^3$) were selected from each of the four full binary datasets. The window size of $100\,pixels^3$ was chosen to ensure that it can capture a sufficient number of structural features in the MPL upon visual inspection. The 300 random volumes were selected because 300 volumes of $100\,pixels^3$ are enough to fill each full dataset ($500 \times 800 \times 204$ pixels) over three times, providing sufficient window overlap for computing statistical averages. The 2-point statistics were calculated (via pore–pore auto-correlations on each 3-D binary volume) for each of the 300 volumes and averaged to obtain an "ensemble average" of 2-point statistics for the MPL. The scalar error in 2-point statistics was then calculated with respect to the ensemble average for each of the individual 300 volumes.

This comparison process was repeated for the other datasets that have window sizes of $50\,pixels^3$ and $75\,pixels^3$. The computed scalar statistical error is plotted for each of the four datasets in Fig. 8. As shown for each window size, the average scalar statistical
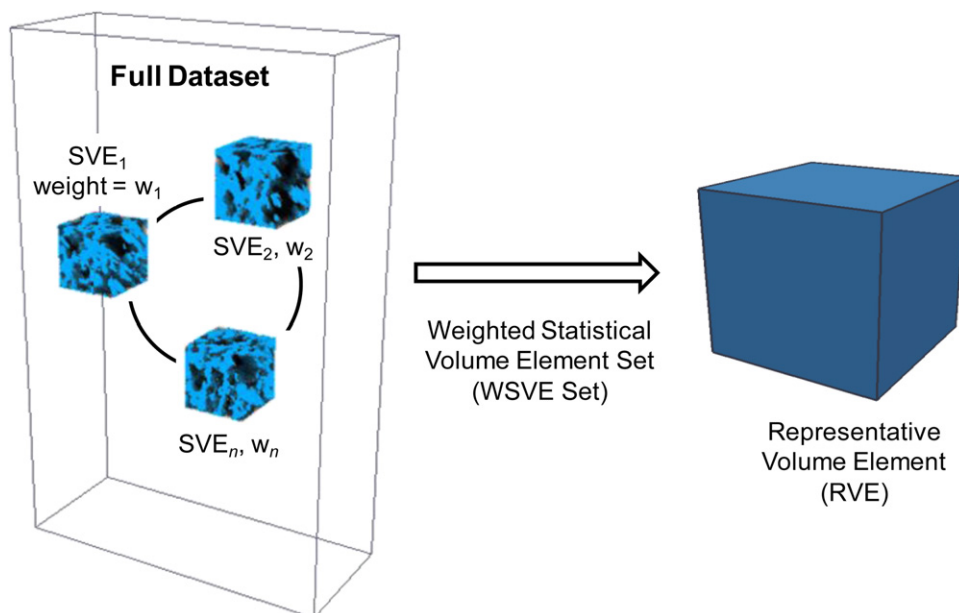

Fig. 6. Schematic of WSVE Set selection from full dataset. A WSVE Set can have different members depending on the structural features of the materials of interest, and it serves as an equivalent of an RVE of the full dataset. An effective value for a given property ("metric") is calculated by taking the weighted average (using the SVE weights, w_n) of the corresponding members of the WSVE Set.

a)

Computed Shortest Tortuous Paths in the Measured Microstructure

b)

$$D_{eff} = K \cdot D_{actual}$$

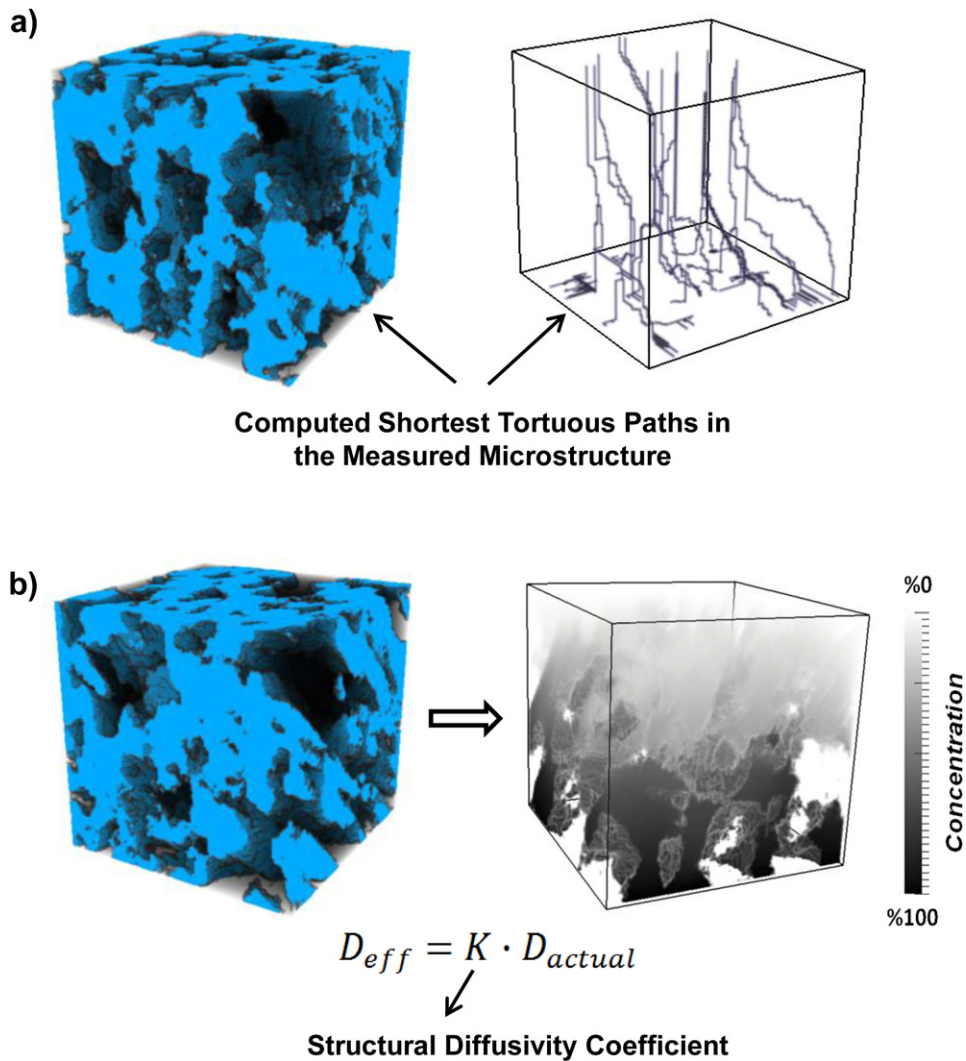**Structural Diffusivity Coefficient**

Fig. 7. Examples of metric (property) analysis of the measured MPL microstructure: (a) tortuosity distribution: shortest path calculations between random pore voxels on the bottom face and the top face [63], and (b) structural diffusion coefficient: the resulting concentration gradient for simulation of diffusion [63]. More information can be found in our study [63].

errors are very close to each other and substantial overlap exists between the error ranges for each dataset, indicating that there is no significant variation in the measured structure between the

Fig. 8. Plot of the average and range of scalar error in 2-point statistics (with respect to the MPL ensemble average) for the random volumes chosen from each of the four datasets. For each dataset-window size combination, 300 random volumes were considered.

four datasets. Therefore, the WSVE Set selection and metric analysis procedures were performed on only one full dataset, which allowed us to save significant computational time without sacrificing from the accuracy.
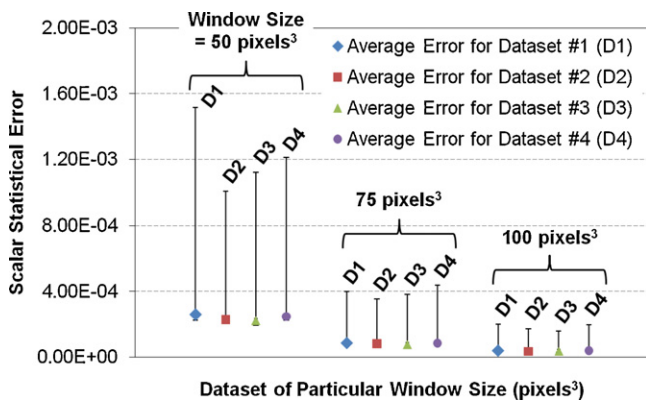
3.2. Selection of WSVE Sets

Prior to selecting a WSVE Set, an appropriate SVE window size and number of SVE members in the WSVE Set should be determined to achieve a proper model domain size for accurate metrics analysis with minimum computational cost. The appropriate SVE window size was determined by performing a procedure similar to the one described in Section 3.1, except it was executed for only one dataset for six different window size cases (50, 75, 100, 125, 150, 175 pixels^3). In each case, the "ensemble average" or target (i.e., the average of 2-point statistics) is calculated from the 300 random volumes in the full dataset for the respective window size. The average and range of scalar statistical error are plotted in Fig. 9 for all six window sizes. As shown in Fig. 9a, a very little drop in error is observed beyond a window size of 100 pixels^3. Thus, a window size of 100 pixels^3 was deemed appropriate for WSVE Set selection to accurately reflect the structural features of the full MPL dataset.
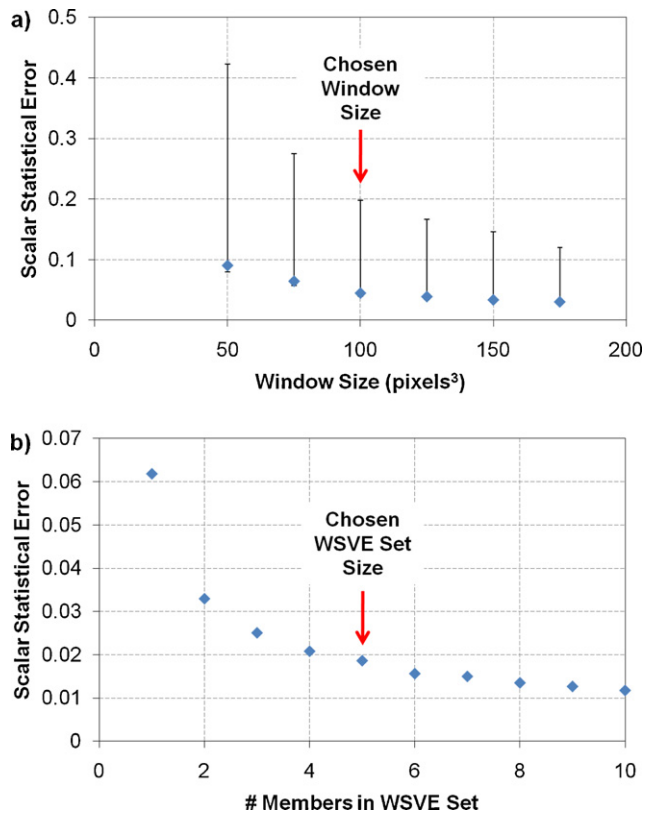
Fig. 9. (a) Plot of scalar statistical error versus window size, for selection of an appropriate SVE window size. Based on the analysis, 100 pixels^3 was determined as the appropriate window size. (b) Plot of scalar statistical error versus number of WSVE members in the WSVE Set, using the selected window size of 100 pixels^3. The 5-member WSVE Set size was observed to be sufficient to capture the structural features of the full MPL dataset.

Once an appropriate SVE window size is identified, the next step is to determine the number of members in a WSVE Set that is necessary to sufficiently capture the structural features of the full dataset. The appropriate number of members in the WSVE Set was determined by finding the WSVE Sets (composed of different numbers of WSVE members, optimally selected from the 300 random volumes) which most accurately reflect the 2-point statistics of the full dataset. For that purpose, WSVE Sets composed of only one member up through ten members (each member has a size of 100 pixels^3) were constructed and evaluated. For each of these ten WSVE Sets, the scalar statistical error in 2-point statistics

between the WSVE Set and ensemble average was determined for comparison. As shown in Fig. 9b, the drop in error beyond a 5-member WSVE Set is observed to be relatively small. This indicates that a WSVE Set having five members seems to be sufficient to accurately capture the structural features of the tested MPL sample. Fig. 10 shows the exact location of each WSVE member within the full MPL dataset for the 1-, 3-, and 5-member WSVE Sets.

3.3. WSVE Sets: metrics and validation

Once a WSVE Set was identified for the material dataset, the metric analysis protocol was applied to determine the key structure and transport metrics for the WSVE Set. For the MPL, this included evaluation of the porosity (ε), internal surface area (ISA), connected internal surface area (CISA), through-plane tortuosity (τ), and the structural diffusivity coefficient (K). For volumes of 100 pixels^3, the codes for determining τ and K each take about 1 h to run on a dual core 2.6 GHz processor with 8 Gb of physical memory. This further justifies our motivation of capturing the structural characteristics of a large microstructure dataset in a small volume (i.e., window size), since the run time scales rapidly with window size.

In order to further optimize the computational time, the metrics for the full dataset were determined by averaging over the 300 random volumes to obtain an "ensemble average". When compared with literature, the computed ensemble average porosity (0.41) and through-plane tortuosity (1.34) results agree very well with the values reported in Ostadi et al. [31], which further validates the microstructure analysis tools introduced in our earlier study [63]. With regards to metric analysis for the WSVE Sets, the metrics of the 1-member, 3-member and 5-member WSVE Sets were determined by scaling the individual metric calculation for each member with the corresponding weighting factor and adding them together to achieve the weighted average. The computed metric values for the full dataset and the 1-, 3-, and 5-member WSVE Sets are shown in Table 1, with % errors included. When the surface area results are compared, a 1-member WSVE Set seems insufficient in terms of accurately capturing the surface area of the full dataset, showing an error around 15% as compared to the full dataset. However, all other metrics are within 5% error for all three WSVE Set sizes.

As with the scalar error in 2-point statistics, the errors in metric calculations are also expected to drop as the number of members in the WSVE Set increases (see Table 1). The results for surface areas (ISA and CISA) follow this trend closely (Fig. 11a), since surface area is closely related to 2-point statistics [65]. Additionally, a loss in surface area of only 1.5 μm^2 μm^{-3} (6.2%) is found when the ISA and
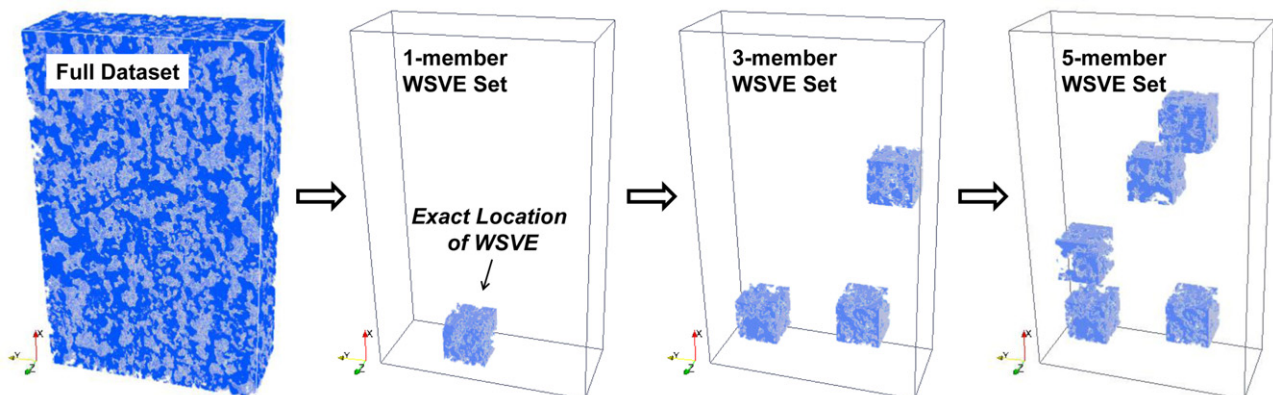

Fig. 10. Exact locations of the members (each member is ~1 μm × 1 μm × 1 μm) of the WSVE Sets within the full dataset (~5 μm × 8 μm × 2 μm) for the 1-, 3-, and 5-member WSVE Sets.

Table 1
Structural properties of MPL obtained from selected WSVE Sets (with different numbers of members) vs. the ensemble average of the full dataset.

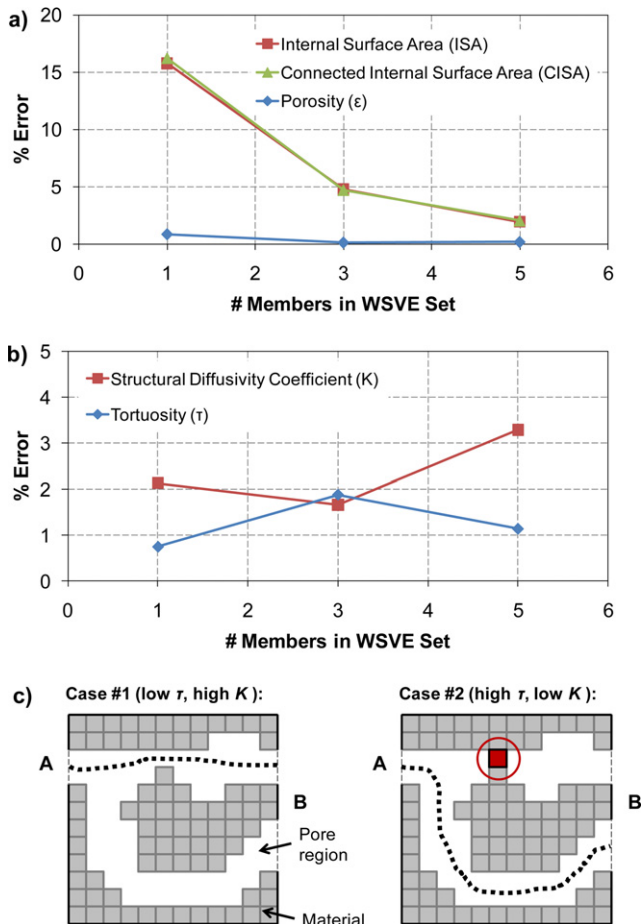|	Porosity	Surface Area ($\mu m^2 \, \mu m^{-3}$)	Connected Surface Area ($\mu m^2 \, \mu m^{-3}$)	Tortuosity	Structural Diffusivity Coefficient
Ensemble average	0.4115	23.77	22.30	1.34	0.225
1-Member WSVE Set	0.4081	27.52	25.91	1.35	0.221
(%Error)	(0.84)	(15.76)	(16.19)	(0.74)	(2.13)
3-Member WSVE Set	0.4110	24.91	23.35	1.37	0.222
(%Error)	(0.13)	(4.76)	(4.70)	(1.88)	(1.66)
5-Member WSVE Set	0.4108	24.23	22.75	1.36	0.218
(%Error)	(0.18)	(1.93)	(2.04)	(1.13)	(3.28)

Fig. 11. Plots of % error with respect to the ensemble average for: (a) ISA, CISA, and ε, showing good convergence to 0% error as WSVE Set size increases; and (b) K and τ, which do not show convergence towards 0% error. (c) Schematics showing the explanation of the behavior of K and τ: For Case #1, the path from A to side B is short (low τ). Adding the circled material pixel in Case #2 drastically increases the path length (i.e., increases τ), but has minimal effect on the 2-point statistics. Adding this pixel will also lower K significantly. Note, K and τ are still within 5% error for the WSVE Sets.

CISA ensemble averages are compared, indicating the existence of a high pore connectivity in the MPL microstructure. Porosity (which is by definition a 1-point statistic) is also well captured by the WSVE Sets. A small increase in % error for the 5-member WSVE Set porosity value is shown in Fig. 11a, but this is likely due to the fact that all 2-point statistics (not just the 1-point statistic) are considered when selecting a WSVE Set. Even so, the WSVE Set porosities are still in very good agreement with the ensemble average, exhibiting negligible % error (less than 1%).

Although quite acceptable, the % errors for tortuosity (τ) and structural diffusivity coefficient (K) do not decrease steadily as the number of members in the WSVE Set increases (Fig. 11b). This behavior is attributed to the fact that τ and K are more complex structure parameters which are most likely related to higher-order statistics (beyond the 2-point statistics). An explanation for this behavior is depicted in Fig. 11c by demonstrating two simple cases. For Case #1, the path from side A to side B in the microstructure is very short, resulting in a low tortuosity (τ). Adding the single material pixel (highlighted in red) to the structure in Case #2 will eliminate the original path/pore region taken, drastically increasing the shortest path length from A to B (i.e., increasing τ) and lowering the K value significantly. However, the addition of this pixel will have minimal effect on the ensemble-averaged 2-point statistics. It should be noted that good agreement for τ and K is still found with respect to the ensemble averages, achieving consistent results well within 5% error for all three WSVE Set sizes (Fig. 11b). These results indicate that the WSVE Set approach is indeed effective in capturing key transport related properties of a microstructure in a small volume to within acceptable tolerance.

To further validate the WSVE Set approach, an investigation was performed in which the 5-member WSVE Set metrics were compared with averages obtained by selecting five random volumes. These random 5-member volume combinations ("sets") were selected from the same 300 random windows used for the WSVE Set selection (Section 3.2). The five random members in each set were weighted equally when computing the metrics, and a total of 5000 of these random volume sets were considered. Histograms composed of computed metrics for the 5000 random 5-member volume sets are shown in Fig. 12. For each metric histogram, a normal distribution fit is applied (shown in red), and the ensemble average of the full dataset and 5-member WSVE Set average are plotted as vertical lines. The ensemble average closely aligns with the peak (mean) of the normal distribution fit, indicating that 5000 random volumes are sufficient for the comparison. When the metrics are compared, the results show that the majority of the 5000 random sets yield metric values which are less accurate than the 5-member WSVE Set. More specifically, the percentage of the 5000 random sets that capture a particular metric of the full dataset *less accurately* than the optimally selected 5-member WSVE Set is 97%, 67%, 61% and 74% for porosity, connected internal surface area, tortuosity and the structural diffusivity coefficient, respectively. This analysis further validates the WSVE Set approach and also emphasizes the importance of the selection of proper representative volume(s) for use in computational models to achieve high accuracy.

3.4. Implementation strategies for different problems

In this work, a case study was performed to demonstrate the ability of the WSVE Set approach to select small representative volumes that accurately represent the prominent morphological features and key transport properties of the full microstructure dataset. Depending on the particular problem under investigation, the size and shape of the RVE or WSVE Sets selected from the full dataset can be tailored to provide an appropriate model domain for property or physical phenomena analysis. For instance, if effective structural or transport properties are desired, it may be sufficient to select a WSVE Set composed of only a few small members (volumes) of cubic shape for property analysis. The property of
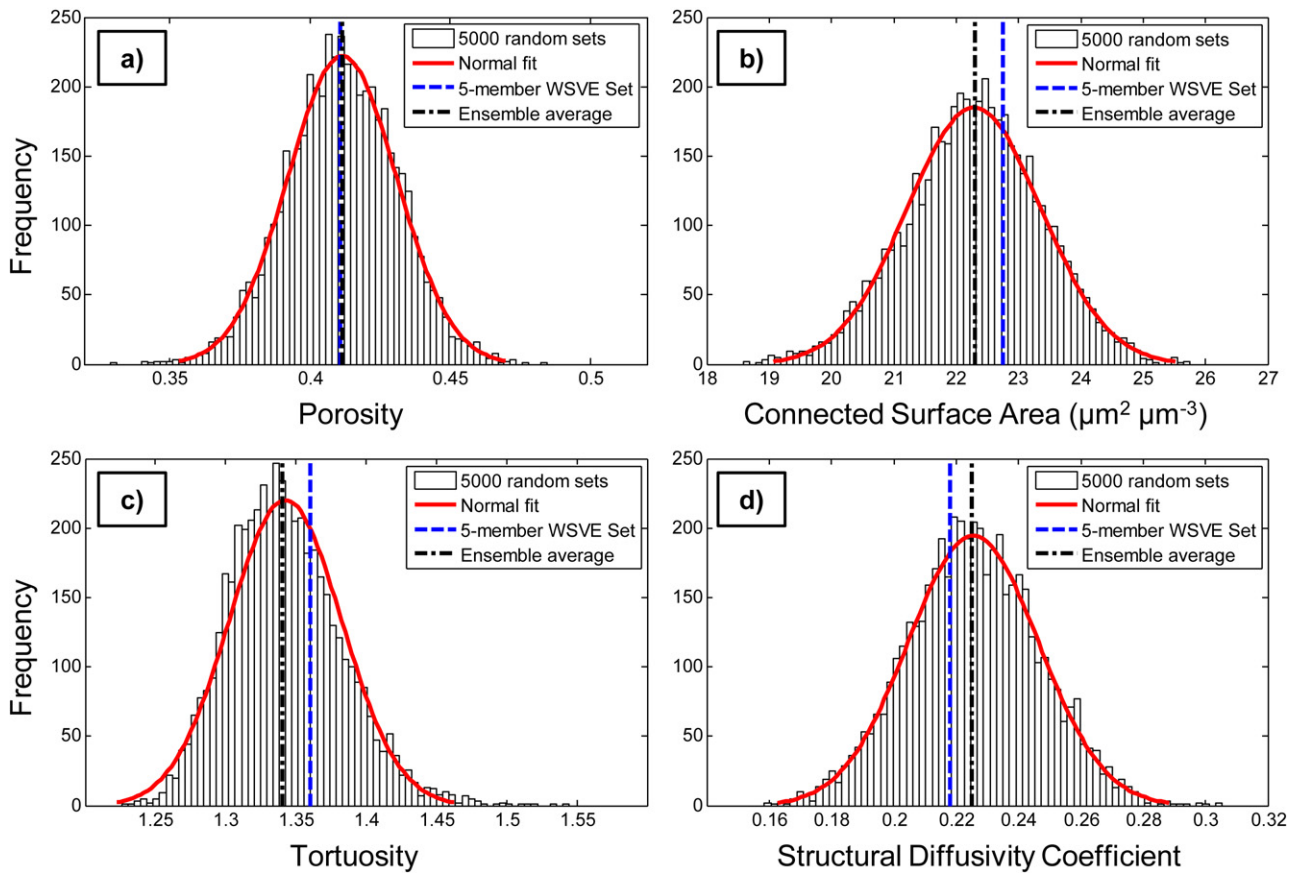
Fig. 12. Histogram plots composed of metric averages for the 5000 random 5-member volume combinations, for (a) porosity, (b) connected surface area, (c) tortuosity, and (d) structural diffusivity coefficient, with a normal distribution fit in red and the ensemble average and 5-member WSVE Set average plotted as vertical lines on each plot. (For interpretation of the references to color in this figure legend, the reader is referred to the web version of the article.)

interest can be computed for these small members of the WSVE Set using a model or microstructure analysis algorithm. The optimally assigned weight of each member in the WSVE Set is then applied to the respective property value, allowing for the determination of the desired property of the material in a computationally efficient manner.

On the other hand, if directionally specific information is desired, such as a temperature, reactant, or liquid water distribution, the dimensions of the WSVE members can be easily controlled during the WSVE Set selection process such that a model domain of proper size is attained. By making the WSVE members longer in the direction of interest, more detail can be captured in that direction to ensure that the desired spatial distribution is sufficiently determined. For example, if one wishes to determine the through-plane water distribution in a DM or catalyst layer, a small WSVE Set could be selected such that the length of each member is equivalent to the thickness of the DM or catalyst layer sample. In this case, the assigned weights of the WSVEs would be applied to their respective distribution to obtain the average through-plane water distribution of the DM or catalyst layer. This approach would be much more effective than performing simulations on the entire dataset which is very computationally prohibitive, or randomly selected regions which may misrepresent the overall structure of the material.

Furthermore, the WSVE Set approach may also be applied to datasets containing more than two phases. For example, consider the catalyst layer of PEFCs, which typically contains four phases: (i) platinum catalyst, (ii) carbon support, (iii) ionomer, and (iv) void (pore) space. In this case, more than one independent 2-point correlation exists. Therefore, more 2-point correlations (both

auto- and cross-correlations) would be considered during WSVE Set selection to sufficiently capture the material structure and phase distribution.

4. Conclusions

In this work, we have presented a new approach for the selection of small RVEs, in the form of WSVE Sets, which accurately capture the prominent features of a much larger material dataset. The approach was applied to a 3-D FIB-SEM dataset for an MPL sample used in PEFCs. Computationally efficient protocols were applied to the MPL dataset to compute the key structure and transport properties that are otherwise very difficult to determine by experimental means.

Small WSVE Sets composed of one, three, and five members (each ~1 μm × 1 μm × 1 μm in size) were selected from the full MPL dataset by matching the overall 2-point statistics of the full dataset. Key structure metrics were evaluated for each WSVE Set and compared with the respective values for the full MPL dataset. The comparison shows very good agreement, indicating that the WSVE Sets can indeed capture structure and transport related properties of the full dataset with high accuracy (less than 5% error). A comparison of the metrics captured for the WSVE Sets against those captured for randomly selected volumes indicates that selection of a random volume from the full dataset will very likely yield a less accurate representation of the overall structure.

In conclusion, the results indicate that WSVE Set approach is an appropriate tool for selecting small, computationally efficient volumes that accurately reflect the salient structural features and transport properties of the much larger, full material dataset. RVEs

identified by this approach can be confidently used in pore-scale fuel cell modeling studies to maximize the computational efficiency and improve the accuracy of model predictions regarding the structure–performance relationship.

Acknowledgements

References

[1] R. Borup, J. Meyers, B. Pivovar, Y.S. Kim, R. Mukundan, N. Garland, D. Myers, M. Wilson, F. Garzon, D. Wood, P. Zelenay, K. More, K. Stroh, T. Zawodzinski, J. Boncella, J.E. McGrath, M. Inaba, K. Miyatake, M. Hori, K. Ota, Z. Ogumi, S. Miyata, A. Nishikata, Z. Siroma, Y. Uchimoto, K. Yasuda, K. Kimijima, N. Iwashita, Chem. Rev. 107 (2007) 3904–3951.
[2] E.C. Kumbur, K.V. Sharp, M.M. Mench, J. Power Sources 176 (2008) 191–199.
[3] K. Jiao, X. Li, Prog. Energy Combust. Sci. 37 (2011) 221–291.
[4] N. Yousfi-Steiner, Ph. Mocoteguy, D. Candusso, D. Hissel, A. Hernandez, A. Aslanides, J. Power Sources 183 (2008) 260–274.
[5] T. Swamy, E.C. Kumbur, M.M. Mench, J. Electrochem. Soc. 157 (1) (2010) B77–B85.
[6] A.Z. Weber, M.A. Hickner, Electrochim. Acta 53 (2008) 7668–7674.
[7] R.P. Ramasamy, E.C. Kumbur, M.M. Mench, W. Liu, D. Moore, M. Murthy, Int. J. Hydrogen Energy 33 (2008) 3351–3367.
[8] U. Pasaogullari, C.Y. Wang, Electrochim. Acta 49 (2004) 4359–4369.
[9] H. Bajpai, M. Khandelwal, E.C. Kumbur, M.M. Mench, J. Power Sources 195 (2010) 4196–4205.
[10] F.E. Hizir, S.O. Ural, E.C. Kumbur, M.M. Mench, J. Power Sources 195 (2010) 3463–3471.
[11] J.T. Gostick, M.A. Ioannidis, M.W. Fowler, M.D. Pritzker, J. Power Sources 173 (2007) 277–290.
[12] M. Rebai, M. Prat, J. Power Sources 192 (2009) 534–543.
[13] K. Lee, J.H. Nam, C. Kim, J. Power Sources 195 (2010) 130–141.
[14] R. Wu, X. Zhu, Q. Liao, H. Wang, Y. Ding, J. Li, D. Ye, Int. J. Hydrogen Energy 35 (2010) 9134–9143.
[15] P.K. Sinha, C. Wang, Chem. Eng. Sci. 63 (2008) 1081–1091.
[16] K. Lee, J. Nam, C. Kim, Electrochim. Acta 54 (2009) 1166–1176.
[17] J. Hinebaugh, A. Bazylak, J. Electrochem. Soc. 157 (10) (2010) B1382–B1390.
[18] J. Hinebaugh, Z. Fishman, A. Bazylak, J. Electrochem. Soc. 157 (11) (2010) B1651–B1657.
[19] R. Benzi, S. Succi, M. Vergassola, Phys. Reports 222 (1992) 145–197.
[20] S. Chen, G.D. Doolen, Annu. Rev. Fluid Mech. 30 (1998) 329–364.
[21] C.K. Aidun, J.R. Clausen, Annu. Rev. Fluid Mech. 42 (2010) 439–472.
[22] X.D. Niu, T. Munekata, S.A. Hyodoa, K. Suga, J. Power Sources 172 (2007) 542–552.
[23] M.A. Van Doormaal, J.G. Pharoah, Int. J. Numer. Methods Fluids 59 (2008) 75–89.
[24] G. Inoue, T. Yoshimoto, Y. Matsukuma, M. Minemoto, J. Power Sources 175 (2008) 145–158.
[25] P.P. Mukherjee, C.Y. Wang, Q. Kang, Electrochim. Acta 54 (2009) 6861–6875.
[26] Y. Tabe, Y. Lee, T. Chikahisa, M. Kozakai, J. Power Sources 193 (2009) 24–31.
[27] P. Zhou, C.W. Wu, J. Power Sources 195 (2010) 1408–1415.
[28] L. Hao, P. Cheng, Int. J. Heat Mass Transfer 53 (2010) 1908–1913.
[29] J. Park, X. Li, J. Power Sources 178 (2008) 248–257.
[30] T. Koido, T. Furusawa, K. Moriyama, J. Power Sources 175 (2008) 127–136.
[31] H. Ostadi, P. Rama, Y. Liu, R. Chen, X.X. Zhang, K. Jiang, J. Membr. Sci. 351 (2010) 69–74.
[32] P. Rama, Y. Liu, R. Chen, H. Ostadi, K. Jiang, Y. Gao, X. Zhang, R. Fisher, M. Jeschke, Energy Fuel 24 (2010) 3130–3143.
[33] P. Quan, B. Zhou, A. Sobiesiak, Z. Liu, J. Power Sources 152 (2005) 131–145.
[34] K. Jiao, B. Zhou, P. Quan, J. Power Sources 157 (2006) 226–243.
[35] Y.H. Cai, J. Hu, H.P. Ma, B.L. Yi, H.M. Zhang, J. Power Sources 161 (2006) 843–848.
[36] B. Mondal, K. Jiao, X. Li, Int. J. Energy Res., (2010), doi:10.1002/er.1776.
[37] K. Jiao, B. Zhou, J. Power Sources 169 (2007) 296–314.
[38] K. Jiao, B. Zhou, J. Power Sources 175 (2008) 106–119.
[39] K. Jiao, B. Zhou, J. Fuel Cell Sci. Technol. 5 (2008) 041011:1–041011:10.
[40] J.W. Park, K. Jiao, X. Li, Appl. Energy 87 (2010) 2180–2186.
[41] E.C. Kumbur, K.V. Sharp, M.M. Mench, J. Power Sources 168 (2007) 356–368.
[42] S.R. Niezgoda, D.M. Turner, D.T. Fullwood, S.R. Kalidindi, Acta Mater. 58 (2010) 4432–4445.
[43] D.T. Fullwood, S.R. Niezgoda, B.L. Adams, S.R. Kalidindi, Prog. Mater. Sci. 55 (2010) 477–562.
[44] S.R. Niezgoda, Stochastic Representation of Microstructure via Higher Order Statistics, PhD thesis, Drexel University, Philadelphia, USA, 2010.
[45] S. Hazanov, C. Huet, J. Mech. Phys. Solids 42 (12) (1994) 5–2011.
[46] C.J. Huet, J. Mech. Phys. Solids 38 (1990) 813–841.
[47] M. Ostoja-Starzewski, Microstructural Randomness and Scaling in Mechanics of Materials, Chapman & Hall/CRC, Boca Raton, FL, 2008.
[48] H. Iwai, N. Shikazono, T. Matsui, H. Teshima, M. Kishimoto, R. Kishida, D. Hayashi, K. Matsuzaki, D. Kanno, M. Saito, H. Muroyama, K. Eguchi, N. Kasagi, H. Yoshida, J. Power Sources 195 (2010) 955–961.
[49] B.J. Inkson, M. Mulvihill, G. Mobus, Scr. Mater. 45 (2001) 753–758.
[50] MATLAB R2010b, The MathWorks Inc., Natick, Massachusetts.
[51] M. Guizar-Sicairos, S.T. Thurman, J.R. Fienup, Opt. Lett. 33 (2008) 156–158.
[52] J.R. Fienup, A.M. Kowalczyk, J. Opt. Soc. Am. A7 (1990) 450–458.
[53] V. Pastushenko, SURFIT, http://www.mathworks.com/matlabcentral/fileexchange/6244, MATLAB Central File Exchange (18 November, 2004).
[54] K.T. Cho, M.M. Mench, J. Power Sources 195 (2010) 6748–6757.
[55] H. Tang, S. Wang, M. Pan, R. Yuan, J. Power Sources 166 (2007) 41–46.
[56] G.H. Ball, D.J. Hall, ISODATA, a Novel Method of Data Analysis and Pattern Classification, Stanford Research Institute, Menlo Park, CA, Technical report AD 699616, 1965.
[57] T.W. Ridler, S. Calvard, IEEE Trans.: Syst. Man Cybern. SMC-8 (1978) 630–632.
[58] D. Ramachandram, Automatic Thresholding, http://www.mathworks.com/matlabcentral/fileexchange/3195, MATLAB Central File Exchange (31 March, 2003).
[59] N. Otsu, IEEE Trans.: Syst. Man Cybern. SMC-9 (1979) 62–66.
[60] S.R. Niezgoda, D.T. Fullwood, S.R. Kalidindi, Acta Mater. 56 (2008) 5285–5292.
[61] S. Torquato, Random Heterogeneous Materials: Microstructure and Macroscopic Properties, Springer, New York, 2002.
[62] A. Tewari, A.M. Gokhale, J.E. Spowart, D.B. Miracle, Acta Mater. 52 (2) (2004) 307–319.
[63] A. Cecen, E.A. Wargo, A.C. Hanna, D.M. Turner, S.R. Kalidindi, E.C. Kumbur, J. Electrochem. Soc., under review.
[64] E.W. Dijkstra, Numer. Math. 1 (1959) 269–271.
[65] J.G. Berryman, J. Math. Phys. 28 (1) (1987) 244–245.